
Article:
Humad, A.M., Provis, J.L. orcid.org/0000-0003-3372-8922, Habermehl-Cwirzen, K. et al. (2 more authors) (2021) Creep and long-term properties of alkali-activated Swedish-slag concrete. Journal of Materials in Civil Engineering, 33 (2). 04020475. ISSN 0899-1561

https://doi.org/10.1061/(asce)mt.1943-5533.0003381

ASCE

Creep and Long-Term Properties of Alkali-Activated Swedish-Slag Concrete

Abeer M. Humad, Ph.D.[1]; John L. Provis[2]; Karin Habermehl-Cwirzen, Ph.D.[3]; Magdalena Rajczakowska[4]; and Andrzej Cwirzen[5]

Abstract: The construction of the future is moving in the direction of environmentally friendly materials and the use of various types of industrial byproducts and wastes. The use of blast furnace slag (BFS) for the production of concrete is one of those alternatives. In this study, pastes and concretes based on high-MgO BFS were alkali activated with 10% by weight sodium carbonate, sodium silicate, and a combination of both. Heat treatment and laboratory curing were applied. The results showed that heat treatment was effective at reducing the drying shrinkage of alkali-activated slag concretes and promoting high early strength. However, the sodium carbonate–activated slag concrete specimens showed a reduction in compressive strength at later ages. All concrete specimens tested exhibited high drying shrinkage; the highest values were for sodium silicate–activated concretes and the lowest were for sodium carbonate–activated concretes. All concretes tested showed very large creep, which was partly related to the small maximum aggregate size (8 mm) and the effects of carbonation. The carbonation depth after 12–24 months was significantly smaller for the heat-treated specimens and for concrete activated with sodium silicate. The carbonation process resulted in a more porous binder matrix, leading to long-term strength loss and increased creep, especially for sodium silicate–activated mixes. **DOI: 10.1061/(ASCE)MT.1943-5533.0003381.**

Author keywords: Alkali-activated slag (AAS) concrete; Shrinkage; Creep of AAS; High-MgO slag; Carbonation.

Introduction

In the last few decades, the global community has shown increasing interest in concretes based on alkali-activated cementitious binders due to their identified environmental, economic, or technical advantages. Alkali-activated binders can be produced from various industrial byproducts, including blast furnace slag (BFS). The hardening processes of alkali-activated BFS binders are to some extent similar to the hydration of high-volume blended BFS/portland cement (PC), but with the addition of a separate activator instead of using PC to elevate the pH and initiate BFS hydration. One of the critical parameters defining the alkali-activated binder solidification process is the pH value of the solution, which is controlled by the alkali activator type. Generally, alkali hydroxides and silicates generate the highest pH values and the highest hydration temperature buildup. Carbonates generate moderately alkaline conditions and lower temperatures and produce free hydroxides through reaction with calcium originating from BFS.

The main hydration product of alkali-activated slag (AAS) is a low-calcium, Al-substituted calcium silicate hydrate (C–A–S–H) gel, together with some or all of hydrotalcite, hydrogarnet, zeolites, alumina, ferric oxide, monosulfate (AFm) phases, and ettringite, depending on the nature of the activator (Wang and Scrivener 1995; Chen and Brouwers 2007; Provis and Bernal 2014). The binding gel contains a relatively high amount of uncombined water compared with the gels formed by PC hydration, which can evaporate during drying, causing considerable shrinkage and microcracking of the binder matrix (Kutti 1992). The AAS concrete binder matrix contains mostly mesopores, while in hydrated PC, capillary pores predominate (Reddy and Tilak 2015). The amount of those pores tends to increase with a higher dosage of alkali activator, leading to greater shrinkage (Häkkinen 1993; Collins and Sanjayan 2000b; Melo Neto et al. 2008). Finer porosity is related to an enhanced hydration degree and greater formation of C–A–S–H phases (Collins and Sanjayan 1999; Bakharev et al. 1999; Krizan and Zivanovic 2002).

The porosity of the C–S–H type gel formed in an AAS matrix has been identified as being higher than is observed in PC-based mixes (Chen and Brouwers 2007). Slag concrete activated with sodium hydroxide showed the highest overall porosity, while sodium carbonate (SC)-activated slag concrete had a porosity comparable to that of PC concrete (Chen and Brouwers 2007). Dry curing increased the porosity and permeability of AAS concrete (Shi et al. 2006). Alkali-activated concretes based on BFS are in some cases characterized by a significantly larger shrinkage than PC-based systems (Collins and Sanjayan 1999, 2000a, b; Cartwright et al. 2015). Shrinkage of AAS binders depends on the pore structure, characteristics of the binding gel, the type and dosage of the alkali activator,

[1]Building Materials Group, Luleå Univ. of Technology, Luleå 971 87, Sweden; Dept. of Civil Engineering, Univ. of Babylon, P.O. Box No. 4, Hillah, Iraq (corresponding author). ORCID: https://orcid.org/0000-0002-5328-4073. Email: abeer.humad@ltu.se; abeer_alasady@yahoo.com

[2]Professor, Dept. of Materials Science and Engineering, Univ. of Sheffield, Sheffield S10 2TG, UK. ORCID: https://orcid.org/0000-0003-3372-8922. Email: j.provis@sheffield.ac.uk

[3]Building Materials Group, Luleå Univ. of Technology, Luleå 971 87, Sweden. Email: karin.habermehl-cwirzen@ltu.se

[4]Ph.D. Student, Building Materials, Structural and Fire Engineering, Dept. of Civil, Environmental and Natural Resources, Luleå Univ. of Technology, Luleå 971 87, Sweden. Email: magdalena.rajczakowska@ltu.se

[5]Professor, Building Materials Group, Luleå Univ. of Technology, Luleå 971 87, Sweden. ORCID: https://orcid.org/0000-0001-6287-2240. Email: andrzej.cwirzen@ltu.se

Note. This manuscript was submitted on August 1, 2019; approved on March 26, 2020; published online on December 3, 2020. Discussion period open until May 3, 2021; separate discussions must be submitted for individual papers. This paper is part of the ***Journal of Materials in Civil Engineering***, © ASCE, ISSN 0899-1561.

the fineness of the BFS, the mixing process, and the curing regime, including relative humidity (Collins and Sanjayan 1999, 2000a, b; Provis et al. 2012; Ye and Radlińska 2016). The binder matrix of AAS is homogeneous but has a finer pore system, which could cause a higher shrinkage, (Melo Neto et al. 2008; Collins and Sanjayan 2000b).

Both drying shrinkage and autogenous shrinkage have been identified as important mechanisms in alkali-activated slags (Shi et al. 2006; Melo Neto et al. 2008). Autogenous shrinkage of AAS concretes has been observed to continue for a longer time and to reach higher ultimate values than ordinary PC (Sakulich and Bentz 2013; Orosz et al. 2019). Drying shrinkage increased with an increased dosage of alkali activator and with increased alkali modulus M_s (SiO_2/Na_2O) of the sodium silicate (SS) activator (Melo Neto et al. 2008; Aydin and Baradan 2012; Humad et al. 2019; Orosz et al. 2019). Activation of BFS by either NaOH or Na_2CO_3 tends to produce drying shrinkage of a similar magnitude to that of PC-based materials (Wang and Scrivener 1995; Collins and Sanjayan 2000b). AAS mixes subjected to heat treatment that are activated with SS with a higher M_s showed intensive cracking (Aydin and Baradan 2012). Prolonged heat curing produced a more mature binder matrix that had greater dimensional stability (Zheng 2010). Shrinkage in PC systems increases with decreasing relative humidity (RH) (Hansen 1987), but conversely, concrete based on AAS has been observed to contract more when exposed to a higher RH, which was explained by the reorganization of the C–A–S–H phase (Ye and Radlińska 2016).

The high drying shrinkage of AAS pastes was related to the structural incorporation of alkali cations in C–A–S–H, which could decrease the stacking regularity of C–A–S–H layers and cause their collapse due to the effect of drying (Ye and Radlińska 2016).

Another phenomenon connected with shrinkage is creep, which is defined as a long-term permanent deformation developing under application of a sustained load. The creep is, similarly to shrinkage, affected by the microstructure of the binder matrix, mechanical properties, aggregate type, and age at loading. The published data related to the creep of alkali-activated materials are rather limited, especially for AAS concrete. Alkali-activated concrete based on a combination of fly ash and BFS showed a lower creep than the comparable PC concrete when cured in ambient laboratory conditions, and a higher creep when sealed (Lee 2007), while the long-term creep of concretes based on AAS tends to be higher in comparison with PC concretes (Ma and Dehn 2017). The creep response of C–S–H type phases is affected by the Ca/Si ratio and the interlayer water. Micro-indentation tests have shown that a lower Ca/Si ratio (0.6–1.5) in this type of phase provided a lower contact creep modulus and led to higher creep values (Zhang et al. 2014; Nguyen et al. 2014).

AAS concrete tends to show a higher strength loss upon carbonation and a greater carbonation depth compared with PC concrete (Bernal et al. 2011, 2012). The carbonation of SS-activated slag caused loss of cohesion of the binder matrix, decreased the compressive strength, and significantly increased the porosity (Puertas et al. 2006; Ghahramani 2017). More recent work has shown that the addition of calcined Mg-Al layered double hydroxide particles can mitigate this drop in strength (Ke et al. 2016). Owing to carbonation, the volume of permeable pores present in the AAS concrete increases contains a higher percentage of capillary pores (Shi et al. 2006; Bernal et al. 2015). Carbonation generated microcracking, which opened the pore system and induced shrinkage (Shi et al. 2006).

The main focus of the research described in this paper was to understand the parameters controlling strength, shrinkage, creep, microstructure, and microchemistry of various types of AAS concretes under long-term exposure and to fill the knowledge gap, particularly in the creep behavior of AAS-based concrete. The slag used to produce these concretes was a high-MgO product from Sweden, which differs significantly in chemistry from most European slag sources, which have a significantly lower MgO content, where the chemical composition of the binder previously has been noted to play a significant role in controlling the reactivity and the reaction products of this particular slag in a way that is not seen in more conventional materials (Humad et al. 2019).

Experimental Setup

Materials

High-MgO-content BFS, type Merit 5000 (MEROX, Oxelösund, Sweden) was used in this study. The chemical composition determined by a PANalytical-Zetium XRF spectrometer and the physical properties of the slag are shown in Table 1. The mix proportions of the concretes studied and compressive strength results are shown in Table 2.

All concretes and pastes contained 450 kg/m^3 of BFS. The water-to-binder ratio (w/b) was 0.45 for all concrete mixes and 0.36 for pastes. Powdered SC provided by CEICH SA Poland, and liquid SS provided by PQ Corporation were used as alkali activators. The SS as-received had a modulus ($M_s = SiO_2/Na_2O$ as a mass ratio) of 2.2 with 34.37% by weight SiO_2, 15.6% by weight Na_2O, and a solid content of 49.97% by weight. The M_s was lowered to 1.0 for use in AAS mixes by an addition of sodium hydroxide (SH) pellets from PQ Corp., 98% purity with 76.31% by weight Na_2O. No plasticizing admixture was used. The total dosage of the solid part of the alkali activator was 10% by weight of the binder weight; similar materials were used previously by Humad et al. (2018). The Jehander Heidelberg Cement Group, Sweden, provided granite aggregates. The total aggregate content (0–8 mm) was 1,663 kg/m^3 with 80% fine content and a specific gravity of 2,700 kg/m^3. Powdered SC and liquid SS were dissolved into the mix water 24 h before the concretes were mixed. The mixing procedure included 1 min mixing of all dry materials, the addition of water with dissolved activators, followed by mixing for another 3 min using a rotating pan mixer of the type Zyklos-ZZ75HE.

Test Procedures: Fresh Concrete

After mixing, the slump of the AAS concrete mixes was determined following ASTM C143. The initial and final setting times of the AAS pastes were determined following ASTM C191 using a

Table 1. Chemical composition and physical properties of ground granulated blast furnace slag used

Component	Oxide (% by weight)	Physical property	Value
CaO	30.4	Specific surface (cm^2/g)	4,500
SiO_2	35	Bulk density (kg/m^3)	1,100
Al_2O_3	14.3	Specific gravity	2.95
Fe_2O_3	0.3	—	—
MgO	16.1	—	—
Na_2O	0.6	—	—
K_2O	0.7	—	—
TiO_2	2.8	—	—
MnO	0.5	—	—
SO_3	0.7	—	—
Loss on ignition	0.9	—	—

Table 2. Mix proportions and curing conditions

Mix ID	Binder content (kg/m^3)	Total w/b ratio	Aggregate content (0–8) (kg/m^3)	Activator dosage as solid material percent by weight of binder	pH of solution	Curing condition	28-day f_{cu} MPa (cube)	28-day f'_c MPa (converted to cylinder)
SC10 L	450	0.45	1,663	10% SC	11.23	Sealed lab cured in 20°C ± 2°C and 40% ± 7% RH	48	38.4
SC10 H						Sealed heat-cured in 65°C for 24 h	39	31.2
SS10 L	450	0.45	1,663	10% SS $M_s = 1$	13.7	Sealed lab cured in 20°C ± 2°C and 40% ± 7% RH	50	40
SS10 H						Sealed heat cured in 65°C for 24 h	53	42.4
SC5 + SS5 L	450	0.45	1,663	5% SC + 5% SS, $M_s = 1$	13.33	Sealed lab cured in 20°C ± 2°C and 40% ± 7% RH	47	37.6
SC5 + SS5 H						Sealed heat cured 65°C for 24 h	49	39.2

Vicat apparatus. The specimens for compressive strength testing were cast in alkali-resistant polymer 100-mm cube molds. Immediately after casting, the samples were sealed against evaporation using plastic bags. Two types of curing procedures were applied: (1) sealing of specimens and storage at 20°C ± 2°C and 40% ± 7% RH until testing; and (2) specimens were sealed and heat cured at 65°C for 24 h, followed by storage (sealed) in lab conditions until testing.

Test Procedures: Hardened Concrete

Compressive strength values were obtained as the average of three 100-mm cubes at 3, 7, 28, 180, and 360 days following the standard SS-EN 12390-3 and using a Toni Technik compressive strength machine. The loading rate was set to 10 N/s.

For drying shrinkage testing, three concrete cylinders with a diameter of 100 mm and height of 200 mm were produced for each mix. The specimens for drying shrinkage measurements were sealed only until final setting (2–3 days) in lab conditions, or for 24 h (heat curing in oven), then kept unsealed in lab conditions. The plastic foil wrapping the cylinder molds was removed when the samples solidified and the drying shrinkage measurement could be initiated.

For creep testing, six cylinders were made for each mix. Three of these six replicates were not loaded but used for shrinkage measurements, and the others were loaded for creep measurement. The applied load was set to 40% of the 28-day compressive strength of the cylinders (Table 2). The creep strains were determined by subtracting the measured drying shrinkage strains on the nonloaded specimens from the strains measured on the loaded specimens.

All samples were stored in laboratory conditions at a temperature of 20°C ± 2°C and 40% ± 7% RH; the samples were sealed for 28 days, and then the sealing was removed. Strain values were recorded using an electronic manual strain gauge, DEMEC type (Mayes Instruments, Vansittart Estate, UK) (Fig. 1). Two pairs of stainless-steel studs were glued with epoxy resin on the specimen surfaces to give a gauge length of 100 mm. The creep test rig consisted of two steel plates connected with adjustable steel rods. Cylinder surfaces were ground flat, and samples were placed in stacks of three in the loading rig (Fig. 2). The load was applied at the age of 28 days using a NIKE hydraulic jack with a maximum oil pressure of 70 MPa. After the desired load was achieved, nuts on the connecting threaded rods were locked. On the next day, the load values were checked and adjusted. Creep and shrinkage values were recorded every day for the first 2 months and every week for the following 2 months. Later values were recorded once a month. The shrinkage strain ε_{sh} value was calculated based on an average value of six replicate readings following Eq. (1) [ACI Committee 209 (ACI 2008)]:

$$\varepsilon_{sh} = 1/6 \sum_{1}^{6} (L_i - L_0)/L_0 \quad (1)$$

where L_i = measured distance between pair of gauge points in micrometers; and L_0 = initial distance between pair of gauge points measured immediately after demolding.

Fig. 1. Strain gauge and specimens for drying shrinkage test.

Fig. 2. Creep setup.

The actual creep ε_c values were calculated following ASTM C512, where the drying and the autogenous shrinkage were extracted [Eq. (2)] [ACI Committee 209 (ACI 2008)]:

$$\varepsilon_c = \varepsilon_t - \varepsilon_{sh} = 1/6\left\{\sum_1^6[(L_{i,t} - L_{0,t})/L_{0,t}) - \sum_1^6(L_{i,sh} - L_{0,sh})/L_{0,sh})]\right\} \quad (2)$$

where ε_c = creep strain; ε_t = total strain including creep and shrinkage; ε_{sh} = shrinkage strain; $L_{i,t}$ = distance measurement in creep test; $L_{0,t}$ = initial distance measurement in creep test; $L_{i,sh}$ = distance measured in shrinkage test; and $L_{0,sh}$ = initial distance measured in shrinkage test.

The carbonation depth was determined after 12 and 24 months of storing the shrinkage specimens (cylinders 100×200 mm) under laboratory conditions (20°C ± 2°C and 40% ± 7% RH). Phenolphthalein Deep Purple Indicator was sprayed onto the split concrete surfaces. When the pH value exceeds 9.5, the indicator changes the binder matrix color to dark magenta, while areas having a pH of less than 9.5 retain a natural concrete color because the indicator is colorless.

XRD analysis was conducted on 7- and 28-day-old powdered paste samples using a PANalytical Empyrean XRD unit using Cu Kα radiation, a step size of 0.0262°2θ, and a total scanning time for each sample of 16 min. The raw data were evaluated using HighScore Plus software. A scanning electron microscope (SEM) type JSM-IT100 (JEOL) was used to study the microstructure of 24-month-old samples. Carbonated, semicarbonated, and noncarbonated areas were analyzed using a QUANTAX energy dispersive X-ray spectrometer (EDX) produced by Bruker with ESPRIT version 2 software. The samples for the SEM studies were impregnated with resin and polished using progressively finer grades of a diamond spray. The porosity was analyzed based on backscattered electron BSE-SEM images using ImageJ software. To remove the noise, a median filter with a two-pixel kernel was applied. Then threshold sensitivity analysis was performed to segment the porosity from the rest of the sample. The so-called overlay method was applied according to the procedure of Wong et al. (2006a). The method makes it possible to determine the upper gray-level threshold of porosity based on the cumulative brightness histogram of BSE images (Wong et al. 2006a, b; Yio et al. 2016). Based on the aforementioned calculation, the global threshold values were estimated for each image. Afterward, the images were binarized and the porosity P was calculated as

$$P = \frac{A_p}{A_{tot}} \times 100\% \quad (3)$$

where A_p = pore area in image (white pixel area in binary segmented image); and A_{tot} = total area of sample (sum of all pixels—black and white).

Results and Discussion

Fresh State Properties

Fig. 3 shows the effect of activator type on workability and setting times, as discussed in a previous publication (Humad et al. 2018), and similar trends were also obtained by other researchers (Rajesh et al. 2013). The final setting times of Mixes SS10, SC10, and SC5 + SS5 were 27, 43, and 52 h, respectively. Previous studies indicated that the presence of calcite $CaCO_3$ tends to decrease the viscosity and to elongate the setting time (Shi and Day 1995; Puertas et al. 2006; Bernal et al. 2015).

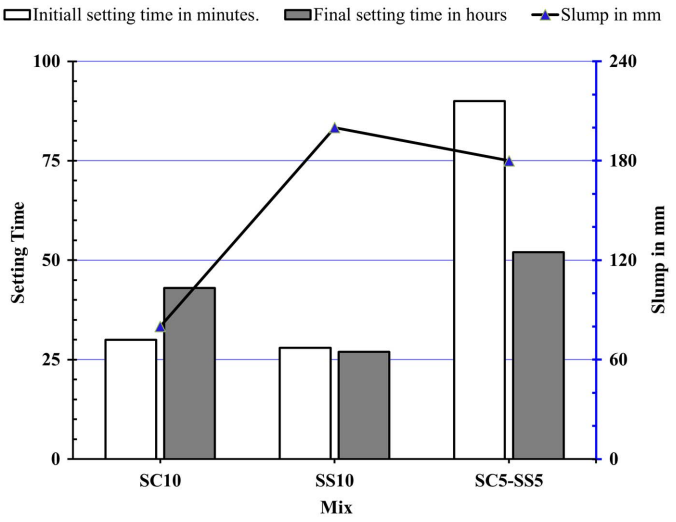

Fig. 3. Initial and final setting time of AAS pastes with slump test results.

Hardened State Properties

Fig. 4 shows the compressive strength development of all mixes at ages of 3, 7, 28, 180, and 365 days. The measured 3-day compressive strength results were higher for the heat-cured specimens due to a more extensive dissolution of the BFS and accelerated formation of binding phases. The 28-day-old SS- and SS/SC-activated slag mixes showed higher compressive strength values than the SC-activated mix, and the SS-activated mix showed the highest strength values with both heat and ambient curing. Similar trends have also been observed by others (Wang et al. 1994; Bakharev et al. 1999; Humad et al. 2018), in connection with the higher extent of reaction. Prolonged curing times tend to enhance the strength development under ambient curing for SS activator owing to the strongly alkaline pore solution, and a similar result was obtained by others (Bernal 2016). However, after 6 months of sealed curing, the mixes containing SC as activator (SC10, SC5 + SS5) showed a reduction in the compressive strength for both heat-treated and non-heat-treated specimens (Fig. 4). A similar trend was observed in PC pastes containing Na_2CO_3 (Janotka 2001) and in heat-cured AAS concretes activated with SS (Bakharev et al. 1999). Decreasing the compressive strength in some AAS mortars has also been observed by other researchers (Bernal 2016), and in some cases the compressive strength stopped developing at about 90 days owing to a lack of moisture required for slag hydration (Collins and Sanjayan 2001). Here, the concrete mixes activated with SS and cured in both regimes (Mixes SS10 L, SS10H) showed only a slight progression in compressive strength values between 6 months and 1 year, but no decrease. The densities of the AAS concretes ranged between 2,220 and 2,300 kg/m^3, and the modulus of elasticity calculated at 28 days increased consistently at higher compressive strengths (Table 3).

The drying shrinkage values measured after 1, 3, 6, and 12 months are also shown in Table 3. The AAS concretes showed rather high values in comparison with the body of literature data for PC concretes, consistent with earlier results (Häkkinen 1993; Collins and Sanjayan 2000a; Reddy and Tilak 2015; Ye and Radlińska 2016). The majority of the heat-cured specimens had a

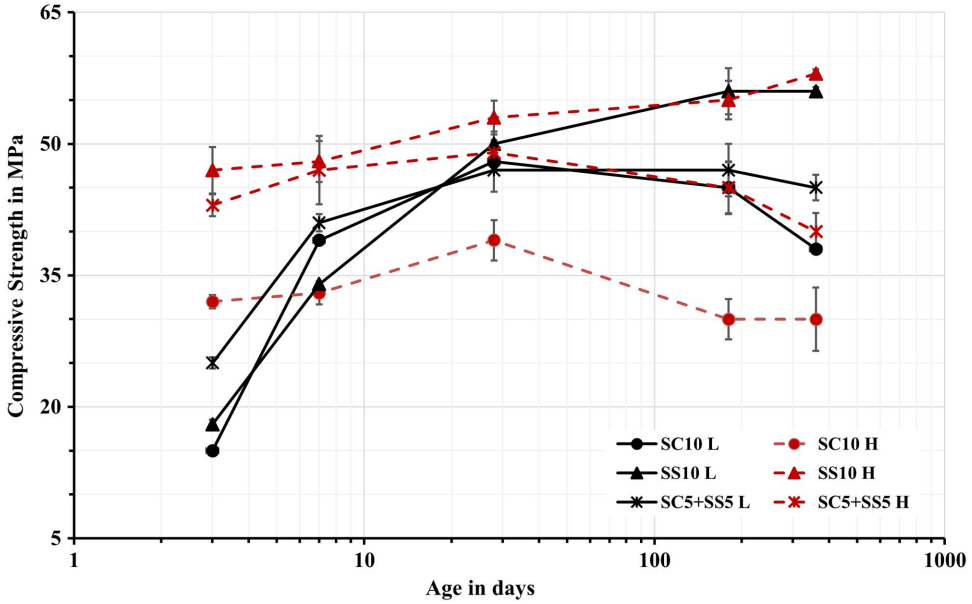

Fig. 4. Progression of compressive strength of cubes during 1 year.

Table 3. Mechanical properties of concretes

Mix ID	ρ (kg/m^3)	E_c of cylinder (GPa)	Creep results: Sustained load (40% of 28-day f'_c) MPa	Creep results: Instantaneous creep strain (mm/m)	Drying shrinkage values (mm/m) at different ages: 1 month	3 month	6 month	1 year	Carbonation depth (mm): 1 year	2 year
SC10 L	2,250	28.7	15.36	0.872	1.81	1.85	1.88	1.95	x	xx
SC10 H	2,296	27.9	12.48	1.048	0.62	1.56	1.78	1.81	21.3	x
SS10 L	2,278	29.8	16.00	1.349	3.06	3.34	3.41	3.48	26.3	34.0
SS10 H	2,221	28.9	16.96	1.704	0.97	2.22	3.28	3.35	13.0	19.8
SC5 + SS5 L	2,233	28.1	15.04	1.043	2.58	2.94	3.06	3.18	31.8	38.8
SC5 + SS5 H	2,262	29.2	15.68	1.033	0.66	1.40	1.85	2.01	20.0	21.5

Note: ρ = density of concrete at 28 days; E_c = static modulus of elasticity of cylinder at 28 days, $E_c = 1.7\rho^2 f_c^{0.33} \times 10^{-6}$ according to BS 8110-2:1985; x = full area (cross section of cylinder 100 × 200 mm) semicarbonated; and xx = full area carbonated.

lower ultimate measured drying shrinkage, mostly because a significant part of the shrinkage is likely to have developed during the first 24 h after casting (24 h, 65°C in an oven) before the start of measurement. Additionally, between the first and third months the measured shrinkage was more than double in the heat-cured versus the lab-cured samples. These results could be related to the higher amount of crystalline phases produced at higher temperature, as revealed in the XRD analysis (Fig. 5). Increasing the amount of crystalline phases due to that increased temperature accelerates the densification of the solid phases within the binder, which leads to a more porous microstructure (Shi et al. 2006). The higher initial rate of hydration tends to retard the next steps in the reaction process as dense reaction products block the availability of slag grain surface for future dissolution, creating a nonuniform distribution of the hydration products and more porous microstructure (Helmuth and Verbeck 1968; Shi et al. 2006). In SC-activated slag pastes more calcite and less gaylussite (Ga) and hydrotalcite-group minerals (HT) were also detected in the heat-cured samples than in the lab-cured one (Fig. 5).

Considering the development of shrinkage over time, 80%–90% of the 1-year shrinkage values were developed during the first 28 days in the case of the non-heat-treated samples, while it took 4 months for the heat-cured specimens to develop the same percentage of their 12-month shrinkage. For comparison, in a typical PC concrete containing 80% by volume of aggregates, having a water-to-cement (w/c) ratio of 0.45 and stored at a RH between 40% and 45% the drying shrinkage values would be 0.5–1.2 mm/m after 1 year (Neville and Brooks 2010). All of the AAS concrete specimens produced in this study, heat-cured and non-heat-cured, showed higher drying shrinkage values than this (1.81–3.48 mm/m). This higher drying shrinkage of the AAS has been linked by other researchers to the structural incorporation of alkali cations in C–A–S–H, which caused the collapse of C–A–S–H layers under drying conditions (Ye and Radlińska 2016), also altering the binder matrix microstructure (Ismail et al. 2013). Typically, AAS contains a larger amount of mesopores than PC concrete, leading to the generation of higher tensile forces during drying, which leads to a higher shrinkage (Häkkinen 1993; Collins and Sanjayan 2000a). The small maximum aggregate size (8 mm) used in these concretes may also be a contributing factor, as is the high binder content of 450 kg/m^3 (Table 2), particularly when considering that the BFS used here is less dense than PC,

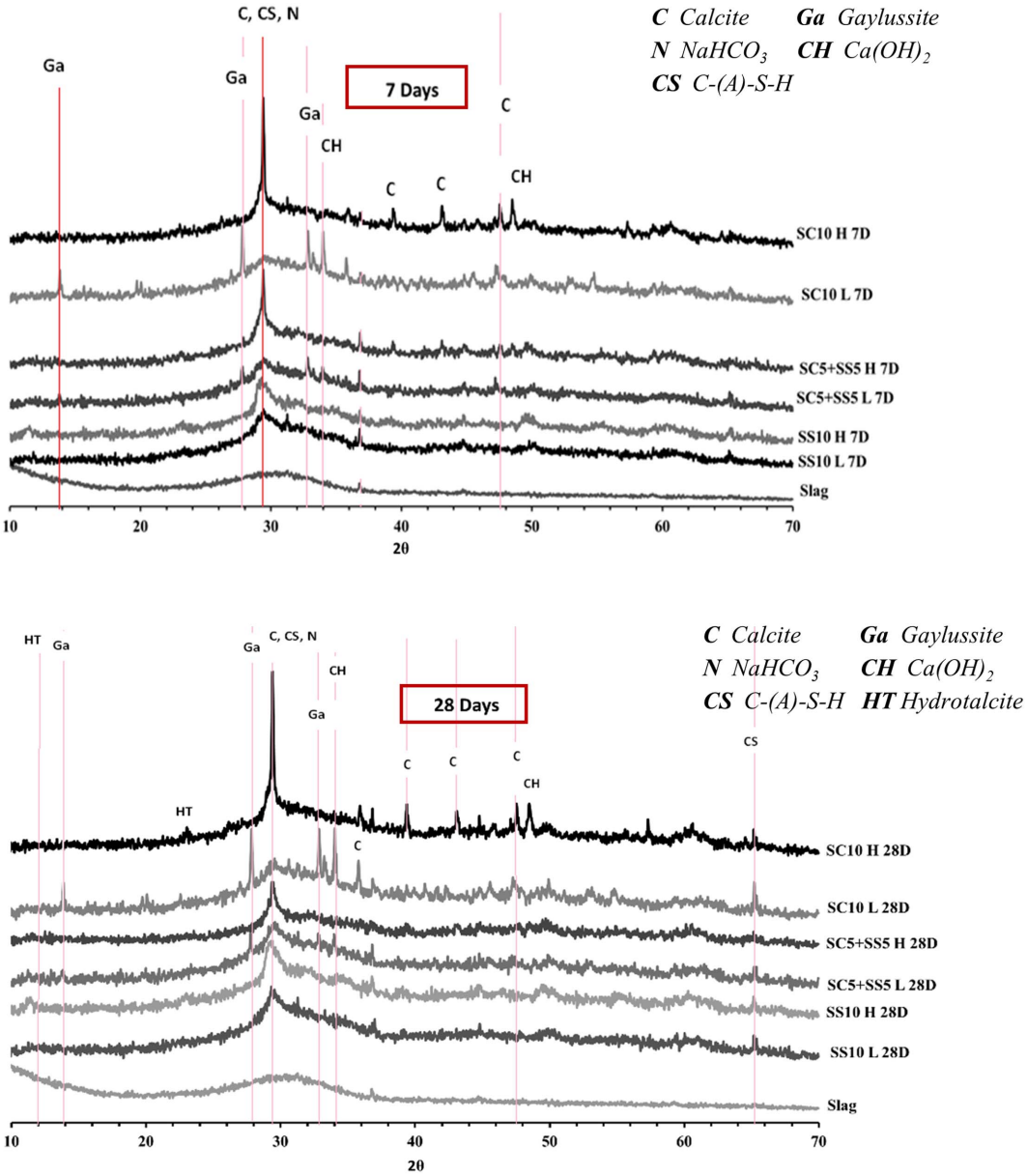

Fig. 5. XRD results for 7- and 28-day cured AAS pastes. Suffixes L7*D* and L28*D* denote 7 and 28 days of lab curing, respectively, whereas *H*7*D* and *H*28*D* denote 7 and 28 days of heat curing, respectively.

so the high binder content on a mass basis becomes particularly notable if converted to a volume basis.

The measured creep values after subtraction of the drying shrinkage are shown in Fig. 6. The instantaneous creep strain (initial strain) was measured immediately after the application of the compression load (Table 3). In addition, creep coefficients and specific creep values were calculated and are shown in Figs. 7 and 8. The creep coefficient was calculated as the ratio of the ultimate creep strain (total creep strain minus drying shrinkage strain) to the initial strain, while the specific creep is the ratio of the creep strain (total creep strain minus drying shrinkage strain minus initial strain) per unit stress [ACI Committee 209 (ACI 2005)]. All concretes activated with SS, which, as described earlier, had the highest drying shrinkage, showed the lowest creep and creep coefficient and the lowest specific creep but the highest instantaneous creep strain. The measured creep values were higher for the heat-treated samples compared with ambient-cured ones, especially for the SS-activated mix (Fig. 6). Similar results were obtained previously for both alkali-activated fly ash concrete and PC concretes (Neville and Brooks 2010; Collins and Sanjayan 1999; Bazant and Li 2008, Wallah and Rangan 2006).

The calculated creep coefficients were nearly identical for heat-treated and non-heat-treated concretes when SS and the combination of SS and SC were used as activators. From these coefficients, the creep strain was approximately two times greater than the initial strain in SS-activated concretes and nine times greater than the initial strain when the combined SS–SC activator was used. Despite the similar 28-day compressive strength values measured for laboratory- and heat-cured mixes, excluding mixes activated with SC, the heat-cured samples showed a higher instantaneous creep (initial strain). This can be related to the more porous binder matrix formed in heat-cured samples. On the other hand, the lab-cured concrete activated with 10% SC showed a higher creep coefficient than the comparable heat-cured samples. The calculated specific

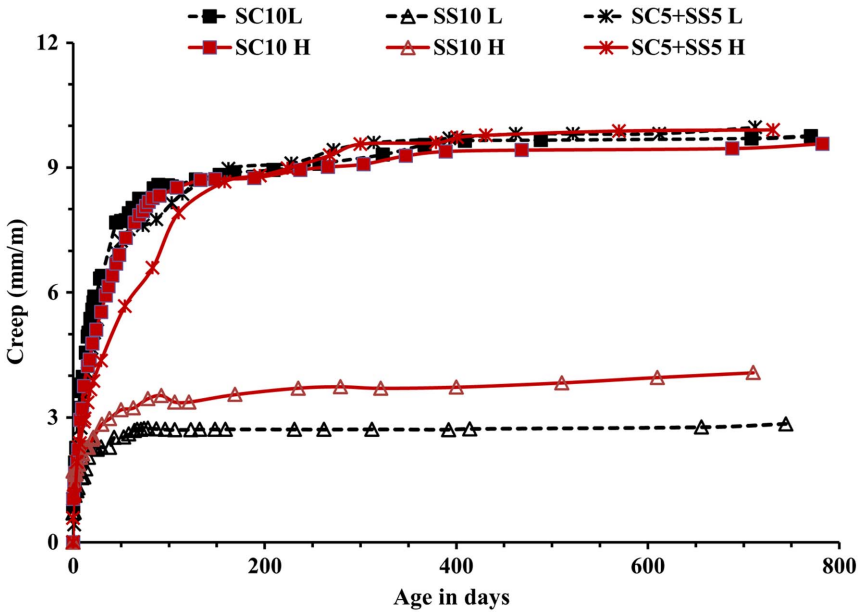

Fig. 6. Creep strain of laboratory- and heat-cured specimens. (Reprinted with permission from Humad 2019.)

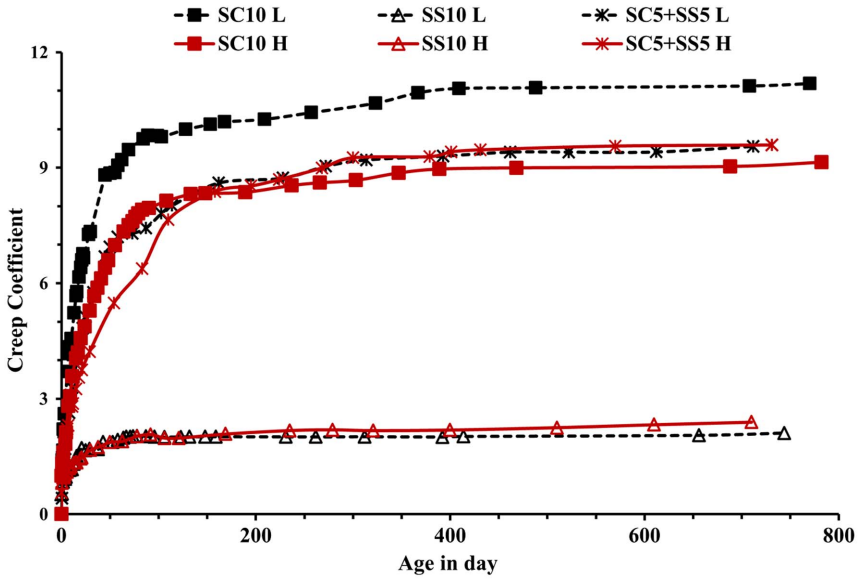

Fig. 7. Creep coefficient of ambient and heat-cured concrete specimens, calculated by dividing creep by instantaneous creep. (Reprinted with permission from Humad 2019.)

creep, which takes into account the compressive strength of the concrete when load is applied (the converted strength to cylinder), was higher for heat-cured samples (Fig. 8). The highest ultimate specific creep was calculated for SC-activated heat-cured concrete. All results can be directly linked to the compressive strength at 28 days, where the mix with a high compressive strength showed a low creep value. In the case of lab-cured mixes activated with 10% SS (Mix SS10L) 90% of the measured creep in 24 months developed during the first 55 days, and 230 days for the heat-cured samples (Mix SS10H). Concretes activated by 10% SC, which showed higher creep, achieved 90% of the ultimate measured creep after about 130 days for both curing types (Mixes SC10L and SC10H). Mixes activated with the combination of SS–SC, for both curing types (Mixes SC5 + SS5 L and SC5 + SS5 H), developed 90% of the total creep after about 160 and 220 days, respectively. All observed trends related to creep can be linked to the microstructure of the binder matrix. Investigation of the concretes by SEM showed significant microcracking (cracks filled with resin), as well as coarsening of the porosity caused by carbonation, and the extent of these effects differed between the various concrete mixes used in the present study. The heat treatment produced a bright rim of hydration product deposited on the surface of the partially hydrated slag particles. Conversely, in lab-cured samples, at later ages, the hydration product deposited was darker in grayscale value (i.e., had a lower atomic number density), especially in the AAS mix containing SS as the activator.

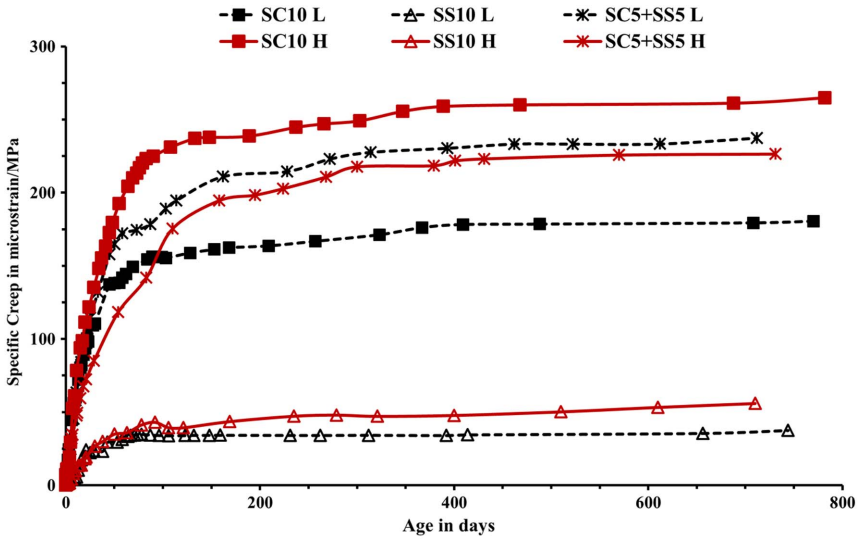

Fig. 8. Specific creep of ambient and heat-cured concrete specimens (specific creep, defined as creep strain per unit stress). (Reprinted with permission from Humad 2019.)

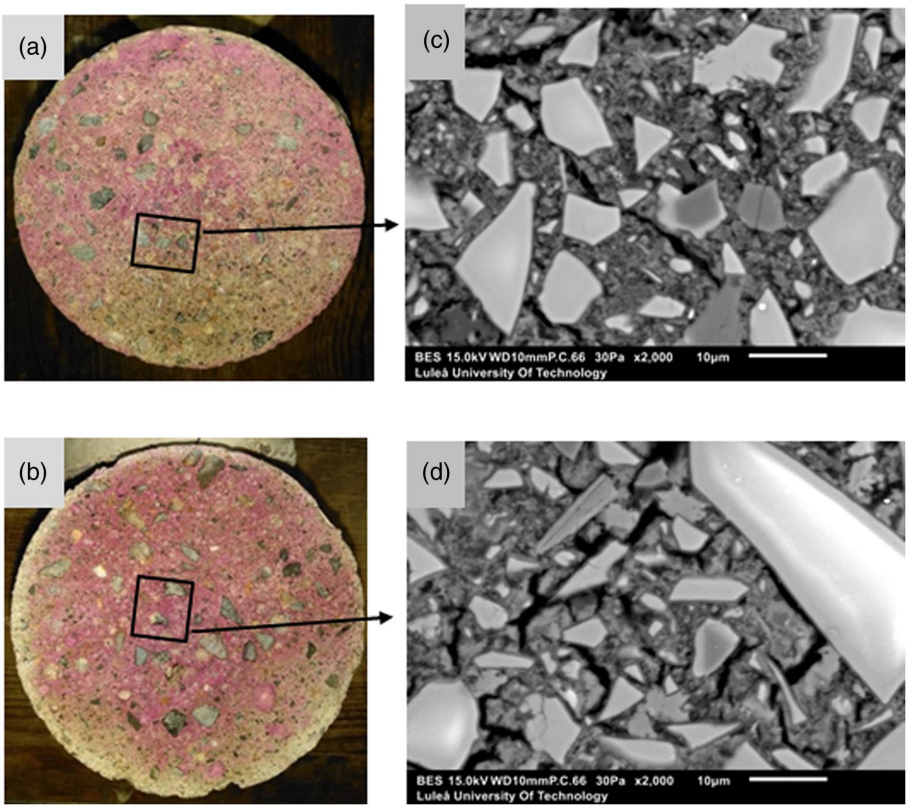

Fig. 9. Carbonation test with phenolphthalein of concrete mixes activated with 10% by weight SC, concrete samples 100 mm in diameter: (a) lab-cured SC10L; (b) heat-cured SC10H; (c) and (d) SEM-BSE images of carbonated region after storage in laboratory environment (20°C ± 2°C and 40% ± 7% RH) for 24 months for SC10L and SC10H, respectively.

High creep values were related to the microcracking evident in the binder matrix (Figs. 9–11). Furthermore, after storing the AAS concrete cylinders in the lab environment (20°C ± 2°C and 40% ± 7% RH), the specimens showed a significant degree of carbonation. Carbonation of AAS concrete is caused by the reaction between CO_2 from the air and the alkaline Na_2O in the pore solution, which causes uptake of carbonate or bicarbonate anions by the decalcification of the C–S–H (Bakharev et al. 2001). The carbonation depths determined by application of phenolphthalein indicator to 12- and 24-month-old samples increased with time (Table 3 and Figs. 9–12). Sealing with plastic bags provided rather good protection against carbonation (Fig. 13). The 24-month-old concretes

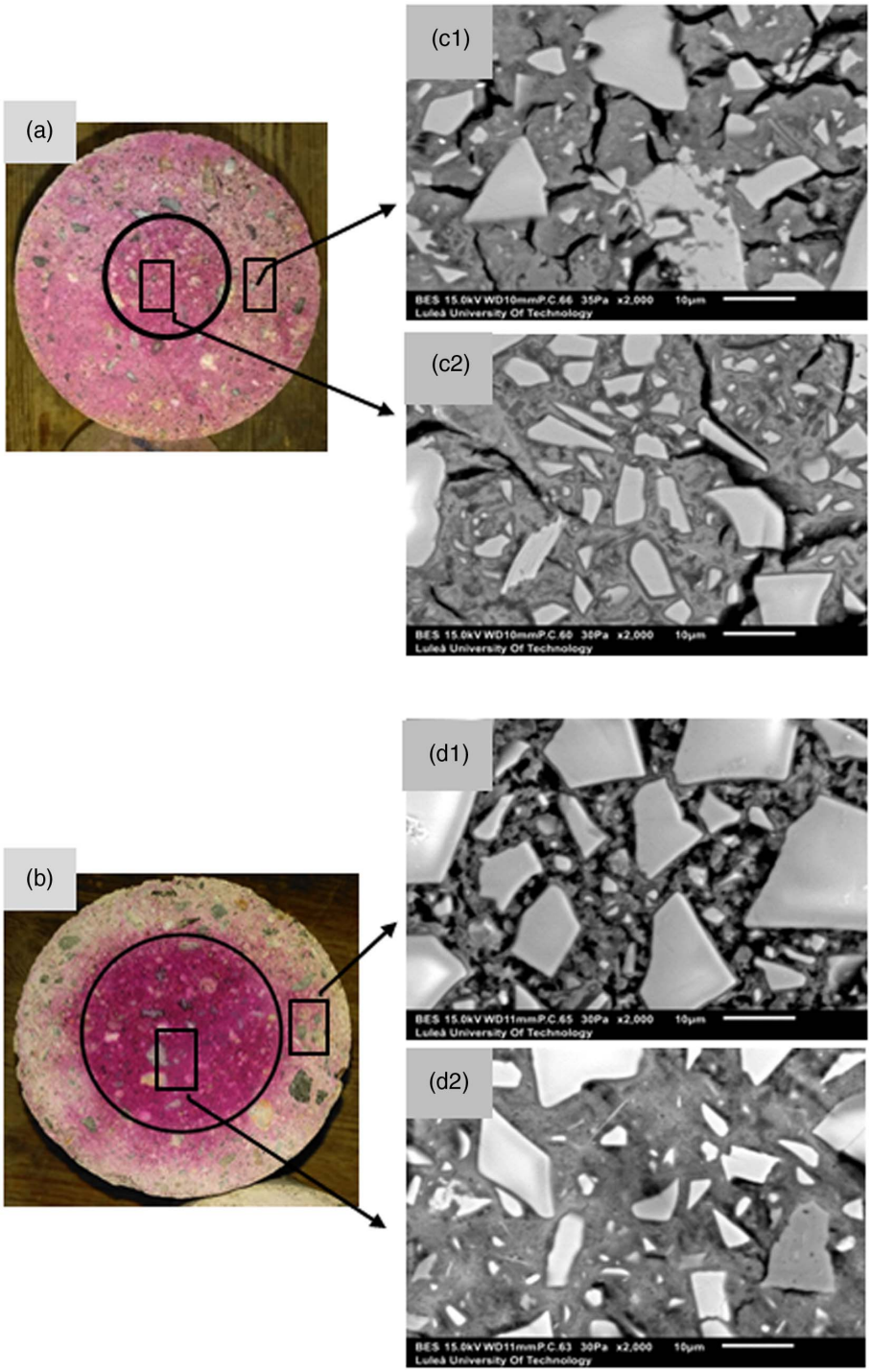

Fig. 10. Carbonation test with phenolphthalein of concrete mixes activated with 10% by weight SS, concrete samples 100 mm in diameter: (a) lab-cured SS10L; and (b) heat-cured SS10H, (C1, 2) and (D1,2) SEM-BSE images of the carbonated region after storage in laboratory environment (20°C ± 2°C and 40% ± 7% RH) for 24 months for SS10L and SS10H, respectively.

activated with 10% SC, under both curing regimes, showed carbonated and semicarbonated regions with highly cracked areas (Fig. 9). A higher porosity of the binder matrix in the carbonated region was observed in Mixes SS10H and SC5+SS5H [Figs. 10(b) and 11(b)]. The calculated total porosity based on segmentation of SEM images is shown in Table 4. The differences can be directly related to the formation of secondary products, which in the case of concretes based on high-MgO slag are likely to include calcite $CaCO_3$, huntite $CaMg_3(CO_3)_4$ natron $Na_2CO_3 \cdot 10H_2O$, thermonatrite $Na_2CO_3 \cdot H_2O$, and gaylussite $Na_2Ca(CO_3)_2 \cdot 5H_2O$, which have been identified as carbonation products of the various binding phases present in AAS paste (Bernal et al. 2014). Alkali-activated high-MgO slag was reported by others to have a lower carbonation depth than others slags with low MgO content (Bernal et al. 2015). The trend was associated to the absorption of CO_2 by the hydrotalcite-type minerals present, which hindered the process of carbonation of the C–A–S–H (Bernal et al. 2015). In the present study, EDX analysis showed that noncarbonated regions of the

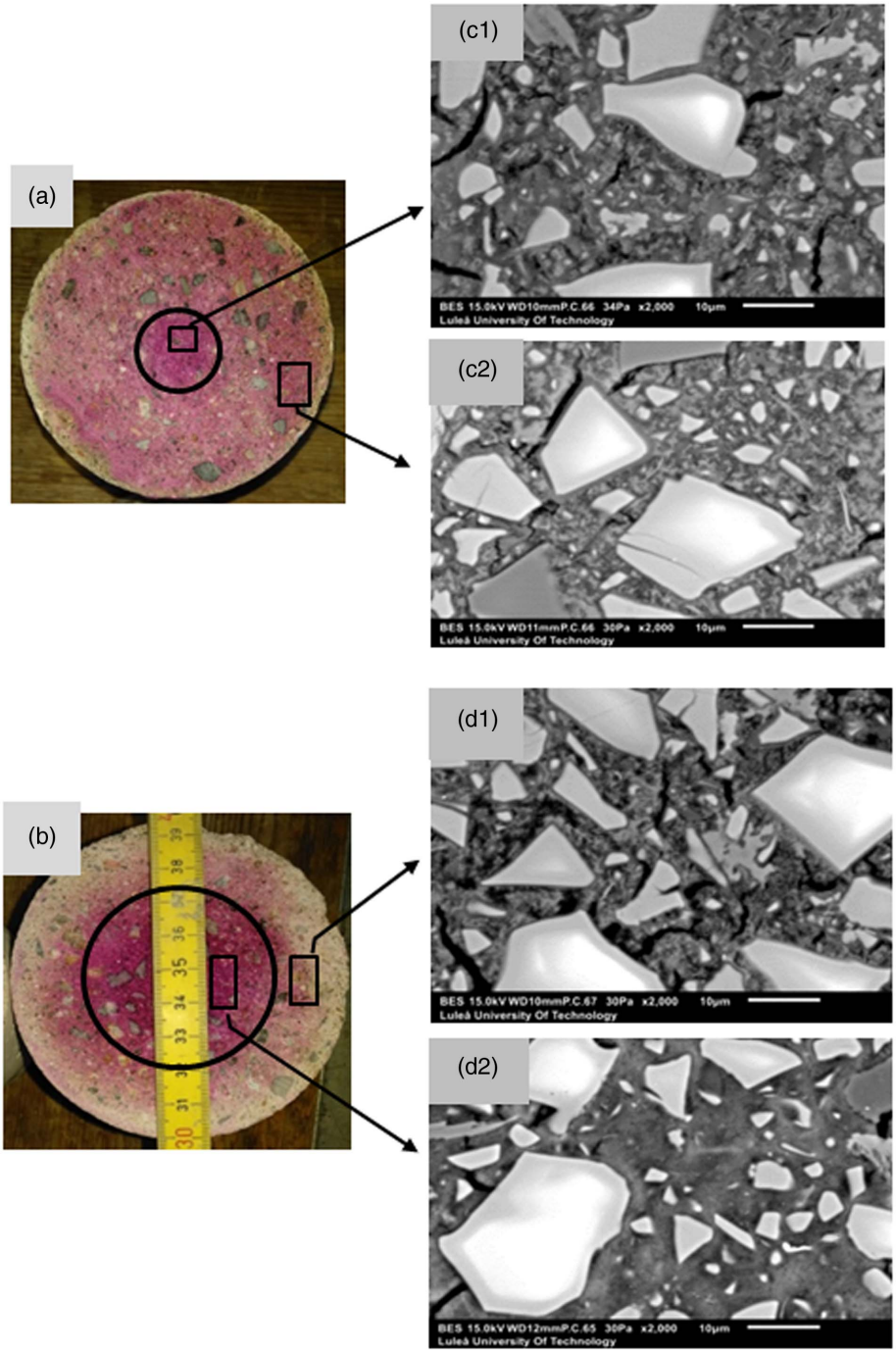

Fig. 11. Carbonation test with phenolphthalein of concrete mixes activated with 5% by weight SC + 5% by weight SS, concrete samples 100 mm in diameter: (a) lab-cured SC10L; and (b) heat-cured SC10H, C1 and C2, and D1 and D2 SEM-BSE images of the carbonated region after storage in laboratory environment (20°C ± 2°C and 40% ± 7% RH) for 24 months for SC5 + SS5 L and SC5 + SS5 H, respectively. (Reprinted with permission from Humad 2019.)

28-day-old AAS concrete contained O, C, Ca, Si, and Al and small amounts of Na and Mg. In contrast, the carbonated regions had lower amounts of Ca, Si, Al, O, Na, and Mg but significantly increased the amount of carbon, which is consistent with the formation of calcium carbonate. The formation of calcium carbonate was also confirmed by an increased Al/Ca ratio and a decreased Si/Ca ratio observed in the carbonated matrices (Fig. 14). Carbonated C–S–H is also identified as weaker, resulting in a higher creep, similar to the results obtained by others (Zhang et al. 2014; Nguyen et al. 2014). Concrete with higher Si/Ca and Al/Ca ratios showed higher creep, similar to the results observed by Nguyen et al. (2014) when the creep was measured with micro- and nanoindentation. The heat-curing procedure appeared to limit the carbonation (Figs. 10–13). Carbonated regions showed a higher extent of deterioration of the microstructure (Table 4 and Fig. 15).

Significantly lower creep strains and creep coefficients than those presented here have been measured for other types of concretes, including high-volume fly ash PC concretes and alkali-activated concretes based on fly ash (Malhotra and Mehta 2002; Wallah and Rangan 2006). The lower creep values of alkali-activated fly ash concretes were related to what those authors called a block-polymerization concept that assumes only

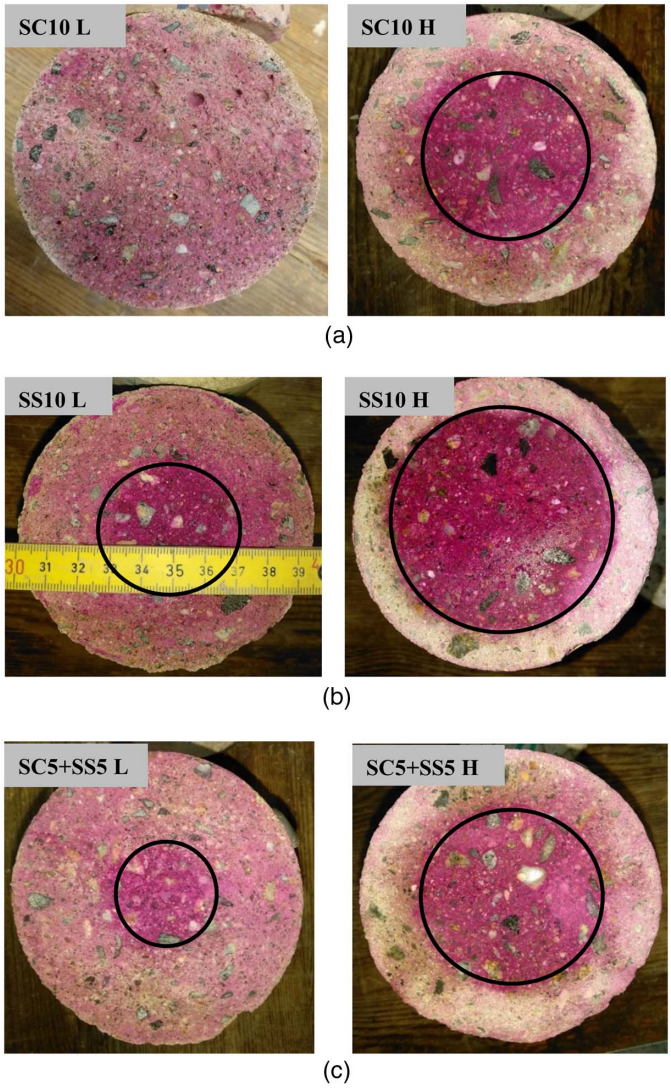

Fig. 12. Phenolphthalein test of carbonation of drying shrinkage concrete specimens (100 mm in diameter) after 12 months of storage in laboratory environment (20°C ± 2°C and 40% ± 7% RH) showing carbonated region as colorless (the external donut area, check with Tables 3 and 4), semicarbonated region with light magenta color (the external donut area, check with Tables 3 and 4), and noncarbonated region with dark magenta (the interior circle area): (a) mixes activated with10% SC lab- (L) and heat-cured (H); (b) mixes activated with 10% SS lab- (L) and heat-cured (H); and (c) mixes activated with 5% SC + 5% SS lab- (L) and heat-cured (H). (Reprinted with permission from Humad 2019.)

partial dissolution of silicon and aluminum from fly ash. Consequently, remnant fly ash particles could act as microaggregates and, thus, reinforce the binder matrix (Pacheco-Torgal 2014). However, this concept does not appear to be valid in the case of alkali-activated systems based on slag, which may be related to the irregular/nonspherical shape of slag particles or differences in the binder microstructure between the C–A–S–H–based binders in AAS and the low-Ca alkali aluminosilicate (N–A–S–H) gels that form in alkali-activated fly ash concretes. In addition, the cracked microstructure (only cracks filled with resin, ignoring cracks formed owing to a SEM vacuum) and a maximum aggregate size of only 8 mm could contribute to the higher creep values measured in the present study.

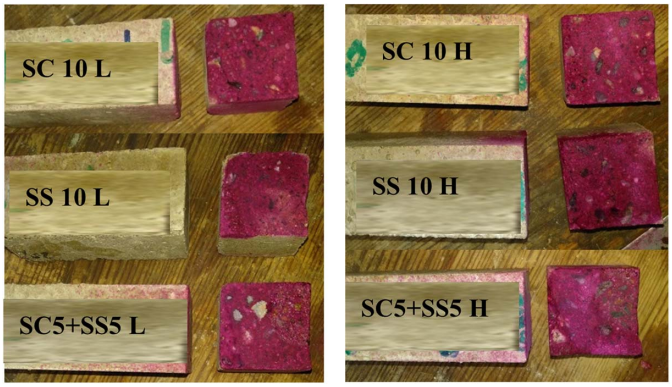

Fig. 13. Carbonation test with phenolphthalein of concrete beam specimens (heat- and lab-cured) after more than 1 year of storage sealed in plastic bags at laboratory environment (20°C ± 2°C and 40% ± 7% RH).

Table 4. Porosity values, calculated using ImageJ software from SEM images after 2 years of exposure to laboratory environment (20°C ± 2°C and 40% ± 7% RH)

	Porosity percentage in different areas	
Mix ID	Carbonated area	Noncarbonated area
SC10 L	9.85	—
SC10 H	9.82	—
SS10 L	10.91 (semicarbonated)	6.63 (semicarbonated)
SS10 H	13.58	4.43
SC5 + SS5 L	7.62 (semicarbonated)	6.22 (semicarbonated)
SC5 + SS5 H	13.97	5.47

Conclusions

1. AAS concrete activated with a combination of SC and SS had better workability, longer initial and final setting times, and higher compressive strength in comparison with concrete mix activated only by SC. High MgO content accelerated the hydration process and produced more rapid strength development.
2. All of the AAS concretes had higher drying shrinkage than comparable PC-based concretes in other studies.
3. Using the heat curing procedure (65°C for 24 h) developed a higher early compressive strength with less progressing in strength between 7 and 28 days old, and decreased the ultimate shrinkage values by accelerating the autogenous shrinkage. Moreover, the researchers found in a previous comparable study (Humad et al. 2019) that increasing the MgO content increased the drying shrinkage values of AAS concrete.
4. Concretes activated with SC showed slight reductions in strength after 6 and 12 months.
5. Alkali-activated concrete based on high-MgO Swedish BFS showed high creep, which could be related to the maximum aggregate size of 8 mm, extensive microcracking of the binder matrix, and the coarsening of the pore structure due to carbonation. However, heat treatment produced higher creep values owing to the formation of a more porous structure.
6. Carbonation of AAS concrete increased the Al/Ca ratio and decreased the Si/Ca ratio and, presumably, weakened the silicate binding gel, especially in the case of heat-cured samples activated with SS. Moreover, high carbonation could be another

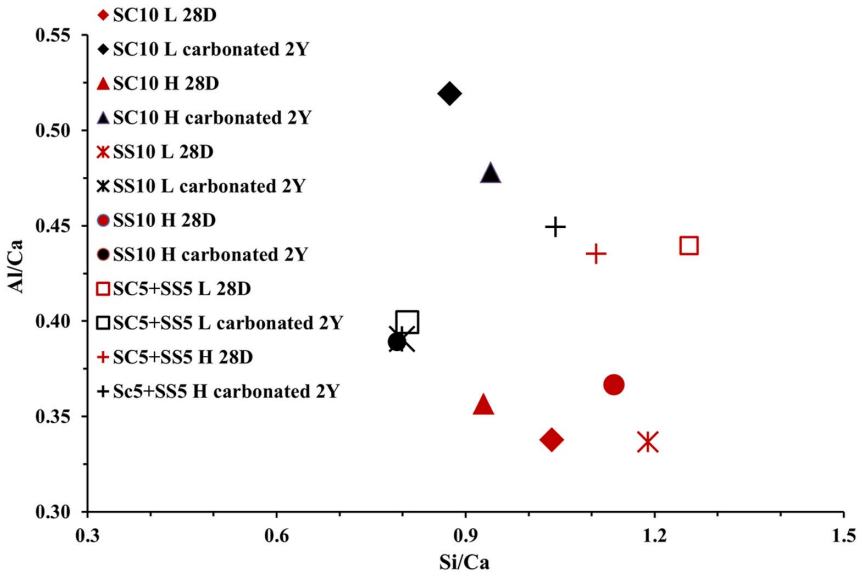

Fig. 14. EDX results showing effect of carbonation on Al/Ca and Si/Ca ratios, where red symbols denote these ratios at 28 days and black symbols denote ratios after carbonation due to 24 months of storage of samples in laboratory environment (20°C ± 2°C and 40% ± 7% RH).

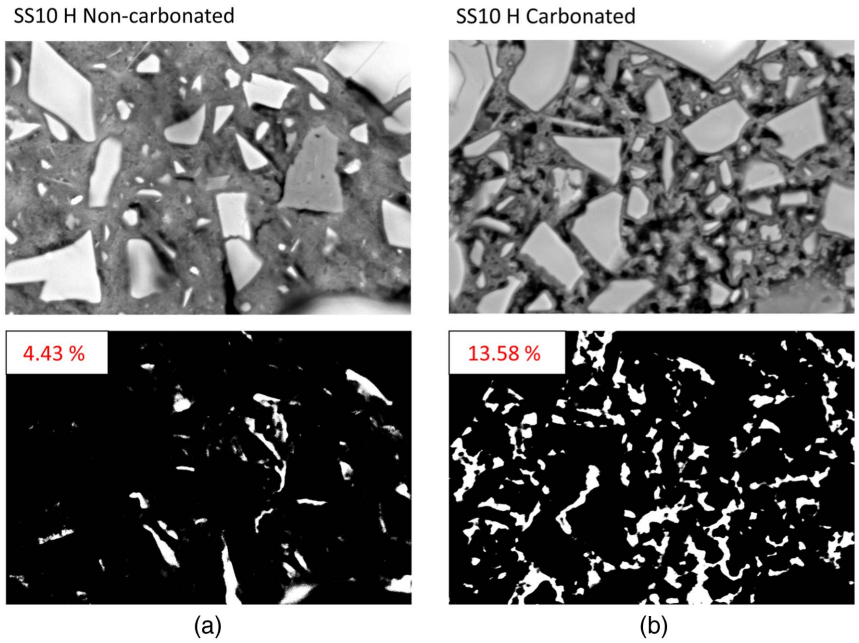

Fig. 15. Porosity percentage segmentation using Image J-software for SEM images of Mix SS10 H after 24 months of exposure to laboratory environment (20°C ± 2°C and 40% ± 7% RH) showing difference in porosity between (a) noncarbonated; and (b) carbonated regions. (Reprinted with permission from Humad 2019.)

reason for the high ultimate drying shrinkage due to carbonation shrinkage.

7. The MgO content controls the formation of secondary phases, such as hydrotalcite, and accelerates the hydration process.

Data Availability Statement

Some or all data, models, or code generated or used during the study are available in an online repository in accordance with funder data retention policies: http://ltu.diva-portal.org/smash/record.jsf?pid=diva2%3A1360129&dswid=2024.

Acknowledgments

This research was funded by the Iraqi Ministry of Higher Education and Scientific Research, Iraq, and the Luleå University of Technology (LTU), Sweden. The authors would like to thank the technical staff of the laboratory at LTU, Sweden.

References

ACI (American Concrete Institute). 2005. *Report on factors affecting shrinkage and creep of hardened concrete*. ACI 209.1R-05. Farmington Hills, MI: ACI.

ACI (American Concrete Institute). 2008. *Prediction of creep, shrinkage, and temperature effects in concrete structures*. ACI 209R-92. Farmington Hills, MI: ACI.

Aydin, S., and B. Baradan. 2012. "Mechanical and microstructural properties of heat cured alkali-activated slag mortars." *Mater. Des.* 35 (Mar): 374–383. https://doi.org/10.1016/j.matdes.2011.10.005.

Bakharev, T., J. G. Sanjayan, and Y. B. Cheng. 1999. "Effect of elevated temperature curing on properties of alkali-activated slag concrete." *Cem. Concr. Res.* 29 (10): 1619–1625. https://doi.org/10.1016/S0008-8846(99)00143-X.

Bakharev, T., J. G. Sanjayan, and Y. B. Cheng. 2001. "Resistance of alkali-activated slag concrete to carbonation." *Cem. Concr. Res.* 31 (9): 1277–1283. https://doi.org/10.1016/S0008-8846(01)00574-9.

Bazant, Z. P., and G.-H. Li. 2008. "Comprehensive database on concrete creep and shrinkage." *ACI Mater. J.* 106 (6): 635–638.

Bernal, S. A. 2016. "Advances in near-neutral salts activation of blast furnace slags." *RILEM Tech. Lett.* 1 (2016): 39–44. https://doi.org/10.21809/rilemtechlett.v1.8.

Bernal, S. A., R. M. de Gutiérrez, A. L. Pedraza, J. L. Provis, E. D. Rodriguez, and S. Delvasto. 2011. "Effect of binder content on the performance of alkali-activated slag concretes." *Cem. Concr. Res.* 41 (1): 1–8. https://doi.org/10.1016/j.cemconres.2010.08.017.

Bernal, S. A., R. Mejía De Gutiérrez, and J. L. Provis. 2012. "Engineering and durability properties of concretes based on alkali-activated granulated blast furnace slag/metakaolin blends." *Constr. Build. Mater.* 33 (Aug): 99–108. https://doi.org/10.1016/j.conbuildmat.2012.01.017.

Bernal, S. A., J. L. Provis, R. J. Myers, R. San Nicolas, and J. S. van Deventer. 2015. "Role of carbonates in the chemical evolution of sodium carbonate-activated slag binders." *Mater. Struct.* 48 (3): 517–529. https://doi.org/10.1617/s11527-014-0412-6.

Bernal, S. A., R. San Nicolas, R. J. Myers, R. M. de Gutiérrez, F. Puertas, J. S. van Deventer, and J. L. Provis. 2014. "MgO content of slag controls phase evolution and structural changes induced by accelerated carbonation in alkali-activated binders." *Cem. Concr. Res.* 57 (Mar): 33–43. https://doi.org/10.1016/j.cemconres.2013.12.003.

Cartwright, C., F. Rajabipour, and A. Radlińska. 2015. "Shrinkage characteristics of alkali-activated slag cements." *J. Mater. Civ. Eng.* 27 (7): B4014007. https://doi.org/10.1061/(ASCE)MT.1943-5533.0001058.

Chen, W., and H. J. H. Brouwers. 2007. "The hydration of slag. 1: Reaction models for alkali-activated slag." *J. Mater. Sci.* 42 (2): 428–443. https://doi.org/10.1007/s10853-006-0873-2.

Collins, F., and J. G. Sanjayan. 1999. "Strength and shrinkage properties of alkali-activated slag concrete containing porous coarse aggregate." *Cem. Concr. Res.* 29 (4): 607–610. https://doi.org/10.1016/S0008-8846(98)00203-8.

Collins, F., and J. G. Sanjayan. 2000a. "Cracking tendency of alkali-activated slag concrete subjected to restrained shrinkage." *Cem. Concr. Res.* 30 (5): 791–798. https://doi.org/10.1016/S0008-8846(00)00243-X.

Collins, F., and J. G. Sanjayan. 2000b. "Effect of pore size distribution on drying shrinkage of alkali-activated slag concrete." *Cem. Concr. Res.* 30 (9): 1401–1406. https://doi.org/10.1016/S0008-8846(00)00327-6.

Collins, F., and J. G. Sanjayan. 2001. "Microcracking and strength development of alkali activated slag concrete." *Cem. Concr. Compos.* 23 (4–5): 345–352. https://doi.org/10.1016/S0958-9465(01)00003-8.

Ghahramani, S. 2017. "Carbonation of alkali-activated slag mortar." Doctoral thesis, Dept. of Civil Engineering, Graduate School College of Engineering, Penn State Univ.

Häkkinen, T. 1993. "The influence of slag content on the microstructure, permeability and mechanical properties of concrete. 1: Microstructural studies and basic mechanical properties." *Cem. Concr. Res.* 23 (2): 407–421. https://doi.org/10.1016/0008-8846(93)90106-J.

Hansen, W. 1987. "Drying shrinkage mechanisms in portland cement paste." *J. Am. Ceram. Soc.* 70 (5): 323–328. https://doi.org/10.1111/j.1151-2916.1987.tb05002.x.

Helmuth, G. J., and R. A. Verbeck. 1968. "Structures and physical properties of cement paste." In Vol. 3 of *Proc., 5th Int. Symp. on the Chemistry of Cement*, 1–32. Berlin: Springer.

Humad, A. M. 2019. "Shrinkage and related properties of alkali-activated binders based on high-MgO blast furnace slag." Ph.D. thesis, Dept. of Civil, Environmental and Natural Resources Engineering, Luleå Univ. of Technology.

Humad, A. M., K. Habermehl-Cwirzen, and A. Cwirzen. 2019. "Effects of fineness and chemical composition of blast furnace slag on properties of alkali-activated binder." *Materials* 12 (20): 3447. https://doi.org/10.3390/ma12203447.

Humad, A. M., J. L. Provis, and A. Cwirzen. 2018. "Alkali activation of a high MgO GGBS: Fresh and hardened properties." *Mag. Concr. Res.* 70 (24): 1256–1264. https://doi.org/10.1680/jmacr.17.00436.

Ismail, I., S. A. Bernal, J. L. Provis, S. Hamdan, and J. S. van Deventer. 2013. "Drying-induced changes in the structure of alkali-activated pastes." *J. Mater. Sci.* 48 (9): 3566–3577. https://doi.org/10.1007/s10853-013-7152-9.

Janotka, I. 2001. "Hydration of the cement paste with Na_2CO_3 addition." *Ceram. Silik.* 45 (1): 16–23.

Ke, X., S. A. Bernal, and J. L. Provis. 2016. "Controlling the reaction kinetics of sodium carbonate-activated slag cements using calcined layered double hydroxides." *Cem. Concr. Res.* 81 (Mar): 24–37. https://doi.org/10.1016/j.cemconres.2015.11.012.

Krizan, D., and B. Zivanovic. 2002. "Effects of dosage and modulus of water glass on early hydration of alkali-slag cements." *Cem. Concr. Res.* 32 (8): 1181–1188. https://doi.org/10.1016/S0008-8846(01)00717-7.

Kutti, T. 1992. "Hydration products of alkali activated slag." In Vol. 4 of *Proc., of 9th international congress on the chimistry of cement*, 468–474. New Delhi, India: National Council for Cement and Building Materials.

Lee, N. 2007. *Creep and shrinkage of inorganic polymer concrete*, BRANZ Study Rep. No. SR 175. Judgeford, New Zealand: Building Research Association of New Zealand.

Ma, J., and F. Dehn. 2017. "Shrinkage and creep behavior of an alkali-activated slag concrete." *Struct. Concr.* 18 (5): 801–810. https://doi.org/10.1002/suco.201600147.

Malhotra, V.M., and P.K. Mehta. 2002. "High-performance, high-volume fly ash concrete." *Suppl. Cem. Mater. Sustain. Develop.* 24 (7): 30–34.

Melo Neto, A. A., M. A. Cincotto, and W. Repette. 2008. "Drying and autogenous shrinkage of pastes and mortars with activated slag cement." *Cem. Concr. Res.* 38 (4): 565–574. https://doi.org/10.1016/j.cemconres.2007.11.002.

Neville, A. M. M., and J. J. J. Brooks. 2010. *Concrete technology*. 2nd ed. London: Pearson.

Nguyen, D. T., R. Alizadeh, J. J. Beaudoin, P. Pourbeik, and L. Raki. 2014. "Microindentation creep of monophasic calcium–silicate–hydrates." *Cem. Concr. Compos.* 48 (Apr): 118–126. https://doi.org/10.1016/j.cemconcomp.2013.11.011.

Orosz, K., A. Humad, H. Hedlund, and A. Cwirzen. 2019. "Autogenous deformation of alkali-activated blast furnace slag concrete subjected to variable curing temperatures." *Adv. Civ. Eng.* 2019: 1–8. https://doi.org/10.1155/2019/6903725.

Pacheco-Torgal, F. 2014. "Introduction to handbook of alkali-activated cements, mortars and concretes." In *Handbook of alkali-activated cements, mortars and concretes*. Sawston, UK: Woodhead Publishing.

Provis, J. L., and S. A. Bernal. 2014. "Geopolymers and related alkali-activated materials." *Annu. Rev. Mater. Res.* 44: 299–327. https://doi.org/10.1146/annurev-matsci-070813-113515.

Provis, J. L., R. J. Myers, C. E. White, V. Rose, and J. S. Van Deventer. 2012. "X-ray microtomography shows pore structure and tortuosity in alkali-activated binders." *Cem. Concr. Res.* 42 (6): 855–864. https://doi.org/10.1016/j.cemconres.2012.03.004.

Puertas, F., M. Palacios, and T. Vázquez. 2006. "Carbonation process of alkali-activated slag mortars." *J. Mater. Sci.* 41 (10): 3071–3082. https://doi.org/10.1007/s10853-005-1821-2.

Rajesh, D. V. S. P., R. A. Narender, T. A. Venkata, and M. Raghavendra. 2013. "Performance of alkali activated slag with various alkali." *Int. J. Innovative Res. Sci. Eng. Technol.* 2 (2): 378–386.

Reddy, A. N., and U. V. Tilak. 2015. "Drying shrinkage and durability studies on alkali activated slag concrete using different activators." *Int. J. Innovative Res. Sci. Eng. Technol.* 4 (11): 11483–11492. https://doi.org/10.15680/IJIRSET.2015.0411116.

Sakulich, A. R., and D. P. Bentz. 2013. "Mitigation of autogenous shrinkage in alkali activated slag mortars by internal curing." *Mater. Struct.* 46 (8): 1355–1367. https://doi.org/10.1617/s11527-012-9978-z.

Shi, C., and R. L. Day. 1995. "A calorimetric study of early hydration of alkali-slag cements." *Cem. Concr. Res.* 25 (6): 1333–1346. https://doi.org/10.1016/0008-8846(95)00126-W.

Shi, C., P. V. Krivenko, and D. Roy. 2006. *Alkali-activated cements and concretes*. Boca Raton, FL: CRC Press.

Wallah, S. E., and B. V. Rangan. 2006. *Low-calcium fly ash-based geopolymer concrete: Long-term properties*. Rep. Perth, WA, Australia: Curtin Univ. of Technology.

Wang, S. D., and K. L. Scrivener. 1995. "Hydration products of alkali activated slag cement." *Cem. Concr. Res.* 25 (3): 561–571. https://doi.org/10.1016/0008-8846(95)00045-E.

Wang, S. D., K. L. Scrivener, and P. L. Pratt. 1994. "Factors affecting the strength of alkali-activated slag." *Cem. Concr. Res.* 24 (6): 1033–1043. https://doi.org/10.1016/0008-8846(94)90026-4.

Wong, H. S., N. R. Buenfeld, and M. K. Head. 2006a. "Estimating transport properties of mortars using image analysis on backscattered electron images." *Cem. Concr. Res.* 36 (8): 1556–1566. https://doi.org/10.1016/j.cemconres.2006.05.002.

Wong, H. S., M. K. Head, and N. R. Buenfeld. 2006b. "Pore segmentation of cement-based materials from backscattered electron images." *Cem. Concr. Res.* 36 (6): 1083–1090. https://doi.org/10.1016/j.cemconres.2005.10.006.

Ye, H., and A. Radlińska. 2016. "Shrinkage mechanisms of alkali-activated slag." *Cem. Concr. Res.* 88 (Oct): 126–135. https://doi.org/10.1016/j.cemconres.2016.07.001.

Yio, M. H. N., H. S. Wong, and N. R. Buenfeld. 2016. "3D Monte Carlo simulation of backscattered electron signal variation across pore-solid boundaries in cement-based materials." *Cem. Concr. Res.* 89 (Nov): 320–331. https://doi.org/10.1016/j.cemconres.2016.09.008.

Zhang, Z., J. L. Provis, A. Reid, and H. Wang. 2014. "Fly ash-based geopolymers: The relationship between composition, pore structure and efflorescence." *Cem. Concr. Res.* 64: 30–41. https://doi.org/10.1016/j.cemconres.2014.06.004.

Zheng, Y. C. 2010. *Shrinkage behaviour of geopolymers*. Parkville, VIC: Univ. of Melbourne.